J. Fluid Mech. (2002), *vol.* 470, *pp.* 247–268.
DOI: 10.1017/S0022112002002033 Printed in the United Kingdom

The interactive dynamics of flow and directional solidification in a Hele-Shaw cell Part 1. Experimental investigation of parallel shear flow

By M. ZHANG AND T. MAXWORTHY†

Department of Aerospace and Mechanical Engineering, University of Southern California, Los Angeles, CA 90089-1191, USA

(Received 9 May 2001 and in revised form 8 April 2002)

It is recognized that flow in the melt can have a profound influence on the dynamics of a solidifying interface and hence on the quality of the solidified material. To better understand the effect of fluid flow on the interface morphological stability and on the cellular and dendritic growth, directional solidification experiments were carried out in a horizontally placed Hele-Shaw cell with and without externally imposed parallel shear flow. The specimen material used was SCN–1.0 Wt% acetone. The experiment shows that the transient parallel flow has a stabilizing effect on the planar interface by damping the existing initial perturbations. The left–right symmetry of crystal cells was broken by the parallel flow, with cells tilting toward the incoming flow direction. The tilting angle increased with the velocity ratio. The secondary dendrites were found to either not appear or appear much later on the downstream side of the crystal cells. The wavelengths of the initial perturbations and of the cellular interface were insensitive to the imposed flow.

1. Introduction

The directional solidification of a binary alloy in a temperature gradient field is the main technique by which many electronic materials are produced. During the solidification process, the solid/liquid interface may experience a planar to non-planar transition, known as morphological instability. The microstructures of solidified materials are to a large extend determined by the type of interface formed during their manufacture. There have been many theoretical and experimental investigations (Flemings 1974; Kurz & Fisher 1981) on morphological stability to gain insight into interface variation, crystal pattern formation and selection, and hence to obtain better control over the properties of solidified materials. It is recognized that flow in the melt can have a profound influence on the interface dynamics and hence the quality of the solidified materials. In particular, flow affects the heat and mass transfer and causes spatial and temporal variations in melt composition. This results in a crystal with non-uniform physical properties which affect the electronic, optical and mechanical performance of materials. There are two categories of flow within the melt: first, natural convection which is generated by buoyancy, expansion or contraction upon phase change, and thermo-solutal capillary effects; secondly, forced flow, generated

† Author to whom correspondence should be addressed.

by external forcing, such as rotation of the crystal during the Czochralski process. In general, neither type of flow can be avoided and they normally have an adverse effect on the stability of the crystal structures.

Rather than bemoaning the presence of flows of as a source of interfacial instability, Hurle in the 1960s suggested that forced flow in the melt might be used to stabilize the interface. Since then, a number of studies have investigated the coupling effect of various flows on morphological stability. The effect of a boundary layer flow on morphological instability was first studied by Delves (1968, 1971), who considered the imposition of both a parabolic profile and a Blasius boundary layer flow over the interface. He studied the case for a semiconductor such as germanium, and concluded that fast stirring can stabilize the interface to perturbations whose wave vector is in the direction of the fluid velocity. Coriell *et al.* (1984) considered the effect of a plane Couette flow on both the morphological and convective modes and concluded that the effect of the flow was to decouple these two modes. Forth & Wheeler (1989, 1992) studied another boundary flow model: the asymptotic suction boundary layer profile. They showed from asymptotic analysis that the effect of the flow was to generate travelling waves parallel to the flow with a speed proportional to the Reynolds number. The direction of the wave was dependent solely upon the magnitude of the disturbance wavenumber and the partition coefficient. Waves travelled against the direction of flow at low wavenumbers, and in the direction of flow at high wavenumbers. Davis and his colleagues (Brattkus & Davis 1988*a*, *b*; Merchant & Davis 1989*a*, *b*; Schulze & Davis 1995) studied the impact of stagnation-point flow with various features. They found that the flow in the direction of the interface creates a long-wave instability with waves travelling toward the stagnation point. It was also found that a temporally modulated stagnation-point flow was always stabilizing with low-frequency modulation, while always destabilizing at high frequencies. The flow can either stabilize or destabilize the system depending on the frequency and amplitude of the oscillations as well as the material properties. Moreover, they believed that the morphological instability could possibly be eliminated by proper selection of the amplitude and frequency. Few quantitative experiments have been reported on the coupled effect of fluid flow and morphological instability. Huang *et al.* (1993) studied the plane Couette flow over crystal cells and dendrites. The flow was generated by a rotating impeller inside the sample cell driven by a rotating outside magnet. It was found that this flow could greatly enhance the planar stability and even induce cell–planar transition. However, it appears that this was not a well-controlled flow and may also have been unsteady.

In this experimental study, we report on an investigation of a forced parallel shear flow with a directionally solidifying interface. The sample material chosen was the organic alloy succinonitrile–acetone (SCN–acetone). In § 2, we present the experimental apparatus and in § 3, experimental procedures. The experimental data and results are presented and discussed in § 4. In § 5, we summarize and conclude.

2. Experimental apparatus

The sample material used in this experiment consists of the transparent organic alloy (TOA) succinonitrile doped with a dilute concentration of acetone (1.0 Wt%). TOAs are special organic materials which demonstrate similar interfacial characteristics, during solidification, as metallic alloys (Jackson & Hunt 1965). Compared with real metallic alloys, they are transparent and have much lower melting points, thus are much easier and cheaper to handle and allow *in-situ* observation under an

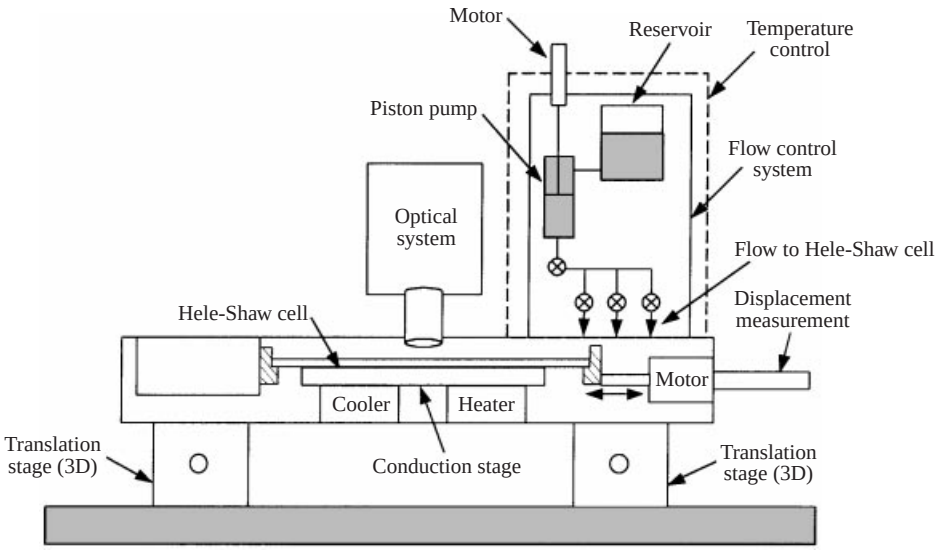

FIGURE 1. Schematic diagram of experimental setup.

optical microscope. The succinonitrile–acetone (SCN–acetone) system is chosen here because the binary phase diagram of this alloy has been precisely obtained and other thermophysical properties have been carefully measured by Chopra, Glicksman & Singh (1988). Moreover, many existing stability analysis results are based on this system (Merchant & Davis 1989*a*, *b*): using SCN–acetone allows a direct comparison of our experimental results with previous analytical work. The sample material SCN used in the experiment is determined to have a purity of greater than 99.9%, by gas chromatography (Sigma Chemical Co.).

The experimental setup (shown in figure 1) is composed of the following parts: Hele-Shaw cell; directional-solidification Bridgeman system; optical system; and flow-control system. Directional solidification of sample materials takes place in the Hele-Shaw cell. Its movement is controlled and measured by the directional-solidification system. The flow-control system was designed to generate different types of flow within the Hele-Shaw cell. These three parts are mounted on a pair of three-dimensional micro-translation stages so that they can move relative to the fixed optical system. The micro-translation stage (Newport MVN80 and 426), with a positioning resolution of 5 μm, allows different parts of the specimen to be put into the field of view.

The Hele-Shaw cell is used to provide a quasi-two-dimensional transparent solidification chamber which makes *in-situ* observations and measurements possible. It consists of two precisely parallel quartz glass plates separated by a small gap (figure 2) in an attempt to eliminate the third dimension from consideration. Each plate is 3 mm thick and ground to optical flatness (less than 1/4 wavelength per in.). The bottom plate is plated with an aluminium reflective coating, which serves as a mirror. The top plate has several groups of holes (1.5 mm diameter) through which liquid alloy can be added or removed. All four sides of the glass plates are sealed with high-performance epoxy (3M DP-420). The Hele-Shaw cell thickness between the two plates is an important parameter in this experiment. If the Hele-Shaw cell is too thick, the temperature and solute concentration variance in the vertical direction and possible thermosolutal convection will make the interface become a complex spatial curved surface instead of a two-dimensional plane (Lan, Chen & Liang 1998). If the

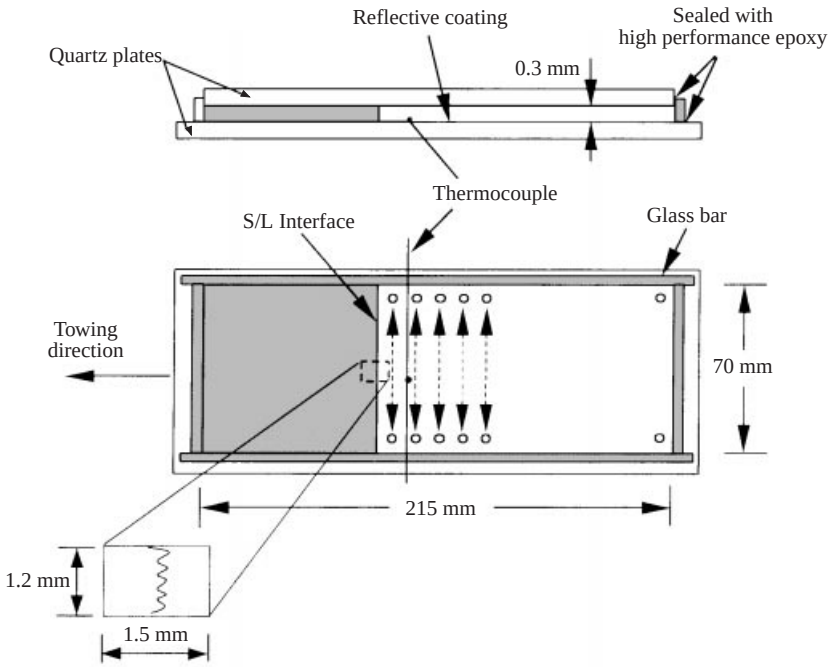

FIGURE 2. Hele-Shaw cell: (*a*) side view; (*b*) top view.

Hele-Shaw cell is too thin, there will be large viscous resistance to the flow. Some experiments (de Cheveigne, Guthmann & Lebrun 1986; Eshelman, Seetharaman & Trivedi 1988) and analytical results (Caroli, Caroli & Roulet 1986) have reported that the critical velocity is dependent on the cell thickness when the thickness is below some critical value (50 μm). It is believed that the solid/liquid meniscus is the cause of this dependence. The interface is curved to satisfy thermodynamic equilibrium (Gibbs–Thomson equation) at the point of contact with glass. For a thickness smaller than the cellular wavelength (typically 50 μm to 200 μm), this curvature effect will be strong enough to break the two-dimensional assumption. Keeping these arguments in mind and after some preliminary tests, we set the Hele-Shaw cell thickness to be 300 μm. This thickness allows flow to move easily through the cell and, at the same time, maintain a simple quasi-two-dimensional interface for planar and cellular growth. The gap spacing and the parallelism of the gap are controlled using stainless steel shims of known thickness. As shown in figure 2, the inside dimension of the Hele-Shaw cell (215 mm by 70 mm) is much larger than the field of view of the microscope (1.5 mm by 1.2 mm). This is a good reason for neglecting the effect of end- and sidewalls.

The Hele-Shaw cell also provides the possibility of imposing well-controlled externally forced flows. Parallel flow is formed by adding liquid into the cell through the holes on one side and removing it through the holes on the other side. The direction of flow can be inverted by switching the source and sink. In the Hele-Shaw cell, there is no free surface and this excludes the possibility of Marangoni flow.

The directional solidification system is based on a horizontal Bridgeman type of furnace. It consists of two horizontally aligned aluminium blocks (heater/cooler pair) with an aluminium plate (conduction bar) mounted on the top and between them (figure 1). Temperatures of the heater/cooler pair are controlled separately by two

water circulators which have temperature stability of 0.01°C. The temperature profile in the conduction bar is considered to be linear except at each end. The temperature gradient is controlled by adjusting the heater/cooler temperatures and/or the distance between them. The Hele-Shaw cell, sitting on top of the conduction bar, can travel back and forth in the towing direction. The temperature distribution inside the cell is detected by an embedded Iron–Constantan thermocouple. One thermocouple is sufficient to cover the temperature field because the two-dimensional Hele-Shaw cell on a Bridgeman furnace can be approximated as a one-dimensional profile near the centre of the Hele-Shaw cell. This one-dimensional temperature field is treated as a steady distribution since the system is moving very slowly (less than $8\,\mu m\,s^{-1}$). As the cell moves from the hot side to the cold side, the thermocouple records the temperatures. If end effects are neglected, the temperature profile obtained this way is equivalent to taking data at different points of the cell at a fixed time. A closed-loop micro-actuator (Newport 850B) is used to drive the directional movement of the Hele-Shaw cell. It has a built-in gearbox with a reduction ratio of 10 : 1. Translation speeds from $3\,\mu m\,s^{-1}$ to $80\,\mu m\,s^{-1}$ can be accommodated by this system to an accuracy of 0.2%. The displacement and speed of the Hele-Shaw cell is measured by a ProScale magnetic encoder attached to the translation stage.

An incident-light microscope (LEITZ Metalloplan) is used to observe the micro-structure of the solid/liquid interface. The whole optical system is mounted on a micro-translation stage so that any part of the specimen can be put into focus. The flow control system is composed of an aluminium reservoir, a piston pump, three stainless steel manifolds and ten nickel-plated brass valves (figure 1). The reservoir is used to contain extra fluid and to prevent bubbles from entering the system. The pump is made of a Teflon cylinder and a stainless steel piston moving inside the cylinder. The piston movement is driven by a Newport 860A Precision Linear Microactuator with $40\,\mu m\,s^{-1}$ to $500\,\mu m\,s^{-1}$ speed range and 0.2% accuracy. As the solid/liquid interface is moving inside the Hele-Shaw cell, different flow channels need to be switched on or off according to the location of the interface. Each channel of flow is formed by turning on the corresponding port of each manifold while leaving other ports closed. All container materials in this system are either Teflon or inert metallic materials (stainless steel, aluminium and coated brass), which have been shown by Rubinstein, Tirmizi & Glicksman (1990) to be chemically compatible with SCN. The flow control system and directional solidification system are placed in a sealed polycarbonate box, whose interior temperature can be adjusted using a thermal control system.

3. Experimental procedures

3.1. *Material preparation and system filling*

A certain amount of SCN is first weighed and heated to the liquid state in a clean, sealed container. A predetermined amount of acetone is added to the liquid SCN and immediately stirred and weighed. The actual concentration of the solution is calculated from these weights, and is calculated to be 1.0 Wt%. The liquid alloy is then introduced into the reservoir through its filling ports while leaving all the valves in the flow control system closed. The alloy is left in the reservoir for more than 10 hours to let the acetone diffuse evenly and to degas any air bubbles. Then each flow channel is opened, one by one, and the liquid alloy is driven by the pump until the whole system, as well as the Hele-Shaw cell, is filled with alloy. Air is vented from two relief holes in the Hele-Shaw cell.

3.2. *Morphological instability: no-flow experiment*

The Hele-Shaw cell was first kept on the hot side of the Bridgeman apparatus for 15 hours to stabilize the solid/liquid interface and distribute solute homogeneously. When the interface became a straight line and small crystals merged into big crystals with crystal size $> 2\,\text{mm}$, the Hele-Shaw cell was towed toward the cold side at a specified speed. Directional solidification ensued as the solid/liquid interface moved toward the liquid side. During this process, the temperature variations were recorded by the thermocouple inside the Hele-Shaw cell, and the interface was observed under the microscope and monitored and recorded by the CCD camera. The experiment was conducted for the no-flow case as a baseline to compare with those with externally applied flows.

The experiment was repeated at different towing speeds between $3\,\mu\text{m}\,\text{s}^{-1}$ and $9\,\mu\text{m}\,\text{s}^{-1}$. Since the interface growing speed was smaller than the applied towing speed, the interface, on the screen, appeared to be moving toward the cold side. Renormalization was needed during experiment to put the interface back into the field of view.

3.3. *Morphological instability: flow experiment*

The parallel flow experiments were conducted under the same conditions as the no-flow ones except for the presence of the flow. Depending upon the time when flow was imposed, they can be categorized into three groups: early-flow, late-flow and steady-flow experiments. For all experiments, the initial concentration C_0 and applied temperature gradient G were fixed. The towing speed, V', and flow speed, U, were varied to give different ratios of U/V'.

Early-flow: The parallel shear flow was turned on when the crystal cell amplitudes were still very small. Since different towing speeds will result in different times to instability and different growth rates, there was no uniform time for all experiments at which the flow was turned on. However, the initial crystal cell amplitudes were smaller than $10\,\mu\text{m}$ for all the experiments.

Late-flow: The flow was turned on at some later time when crystal cells were well developed. The cell amplitude range when the flow was turned on was from $30\,\mu\text{m}$ to $50\,\mu\text{m}$.

Steady-flow: The flow was turned on first. After the flow field and thermal field reached steady state (with no temperature fluctuation being detected), the directional movement of the Hele-Shaw cell was initiated.

4. Results and discussion

The experimental results of the current study are presented in three parts. First, results of pure morphological experiments are discussed, where experimental data can be compared with the linear stability theory of Mullins & Sekerka (1964) (referred to as M-S theory below), and the numerical simulation of Buddhavarapu & Meiburg (2002, part 2 of this work). Then, results obtained from parallel shear flow experiments are presented. These results are compared with those obtained from pure morphological experiments to determine the effects of each type of flow. Specifically, the flow effects focused on are the influence of flow on interface perturbations (wavelength λ and growth rate σ) and interface orientation (cell/dendrite tilting angle θ). Physical mechanisms are presented to partially explain the effect of each flow. Traditionally, flow in Hele-Shaw cell is treated as potential flow, but that flow model is not valid for our directional solidification experiment, because the viscous boundary layer and

concentration boundary layer have similar thickness in all these experimental runs. A strong viscous effect, as detailed in the discussion below, can be observed from flow field visualization as well as from the impact of the flow on interface morphology.

4.1. *Morphological instability experiment*

Once the sample material is chosen, SCN–1.0 Wt% acetone, the morphological number M and surface energy number $\mathscr{A}$ will only depend on interface growth speed V and temperature gradient G:

$$M = \frac{mG_c}{G} = 214.0\frac{V}{G}, \tag{4.1}$$

$$\mathscr{A} = \frac{T_M \gamma V k^2}{mL_V D_L C_\infty (k-1)} = 1.883 \times 10^{-7} V, \tag{4.2}$$

where V is in $\mu m\,s^{-1}$ and G is in $^\circ C\,cm^{-1}$, m is the liquidus slope for SCN–acetone alloy, G_c is the solute concentration gradient at the interface on the liquid side, T_M is the melting point of pure SCN, γ is surface energy, k is the segregation coefficient, L_v is the latent heat per unit volume, D_L is the solute diffusivity, and C_∞ is far-field solute concentration. The horizontal Bridgeman apparatus used in this study can provide a smooth towing speed, V', from $3.0\,\mu m\,s^{-1}$ to $10.0\,\mu m\,s^{-1}$ and a linear temperature gradient G from $1\,^\circ C\,cm^{-1}$ to $13\,^\circ C\,cm^{-1}$. This range of experimental conditions allows the growth speed, V, of the planar interface to change from $0.2\,\mu m\,s^{-1}$ to $3.0\,\mu m\,s^{-1}$.

Figure 3 shows the interface morphology changes in one experimental run as the Hele-Shaw cell is pulled in the direction of negative temperature gradient. The frame code, representing a framing rate of 1/30 s, appears in the right upper corner of each picture. It is started when the Hele-Shaw cell begins to move. Because the morphological number M (6.7) is much larger than the critical value M_c (1.07), the solid/liquid interface changes from planar to cellular to dendritic structures. During the entire process, most crystal cells keep their symmetry and grow in the normal direction of the initial planar interface. After a sufficiently long time, the interface reaches a steady dendritic state with a growth speed equal to the towing speed. It should be noted that a thermal-steady assumption is made in most stability theories (Coriell & McFadden 1993), i.e. the interface is always in an equilibrium state and the actual interface growth speed V is equal to the applied towing speed V' during the entire process. If this assumption holds, the solid/liquid interface should appear stationary under the microscope. During real time experiments, however, the interface is found to move towards the solid side and the microscope needs to be adjusted every few minutes in order to put the interface back into the field of view.

Eshelman & Trivedi (1987) took great care in their experiment to reach the thermal-steady condition and their critical velocity was in good agreement with M-S theory. Our study focuses on the interactive effect of flow and solidification interface. This effect, as shown in the later discussion, appears more obvious on a non-stable interface; therefore all our experiments are carried out under thermal-unsteady condition.

4.2. *Measurement of interface characteristics*

Measured morphological parameters, which will be discussed in this section, include wavelength λ, growth rate σ of the initial perturbations and length of individual

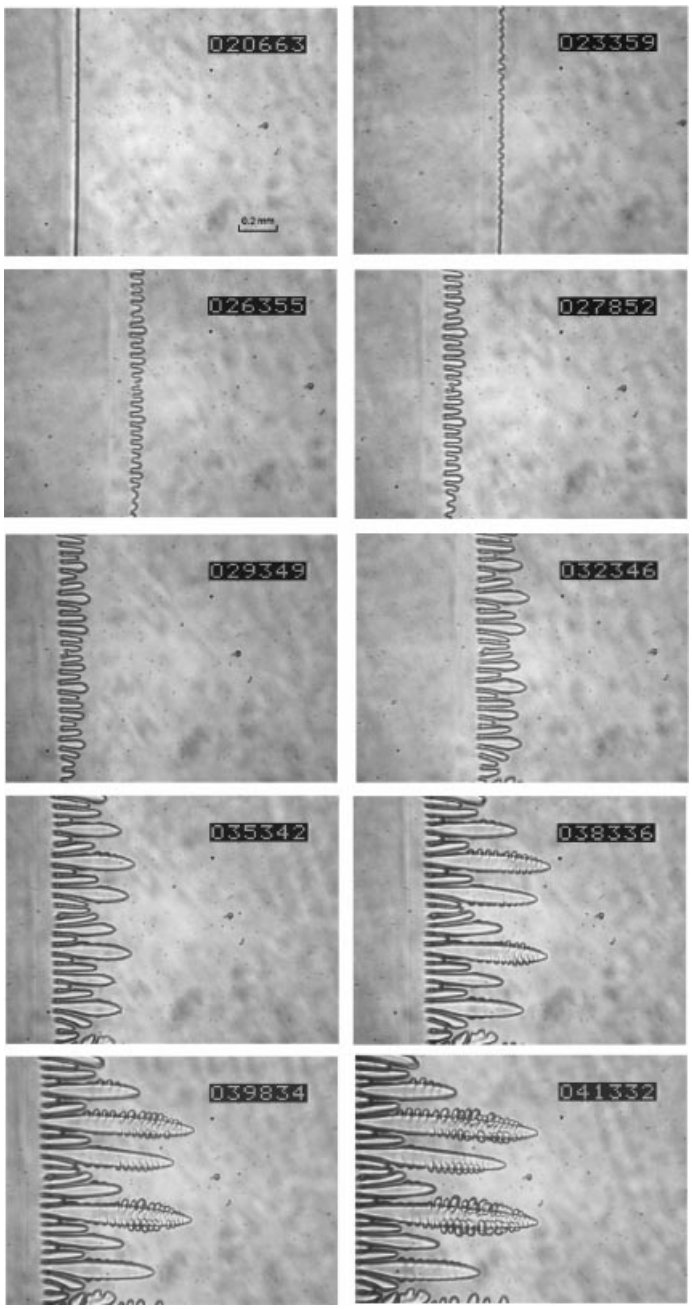

FIGURE 3. Directional solidification: growth with no flow applied ($V' = 3.6\,\mu\mathrm{m\,s^{-1}}$, $G = 7.0\,^{\circ}\mathrm{C\,cm^{-1}}$).

crystal cells L. The measurement of these interface characteristics could have been quite subjective and time consuming. In order to quantify them and to make results of different experiments comparable, objective measurement methods needed to be developed.

Extreme difficulty has been reported associated with measuring the initial perturbations (Lee & Brown 1993). One common method for measuring their wavelength

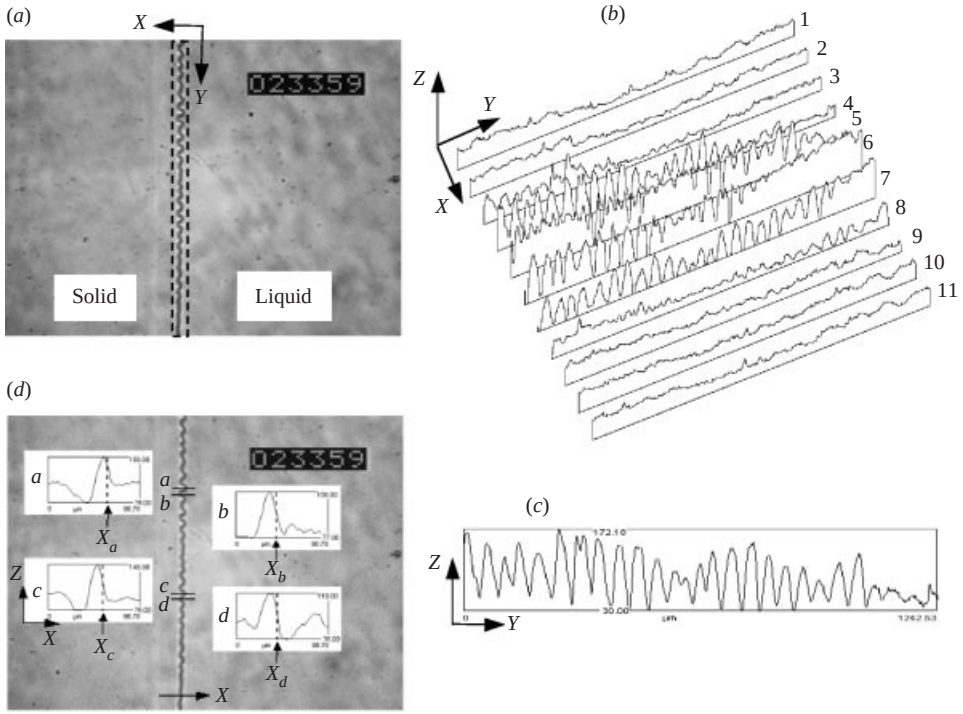

FIGURE 4. Determination of λ and L.

is based on area counting:

$$\lambda = \alpha(S/N)^{1/2}, \tag{4.3}$$

where N is the number of crystal cells within a large area S. The coefficient α, which depends on the nature of the interface, is rather subjectively estimated as a real interface is never perfectly hexagonal ($\alpha = 1.075$), square ($\alpha = 1$), or completely random ($\alpha = 0.5$). Another method is just simply counting the number of crystal cells within a large region. This method works well on an interface with uniformly growing perturbations, yet is unreliable for an interface in a transient state where the growth rates of individual crystal cells are quite different.

The method developed in the present study to determine λ is based on the measurement of grey-scale values. A rectangular region, containing the solid/liquid interface, is first selected for a surface plot, as shown in figure 4(a). Once the size and location of this region is known, then a three-dimensional surface plot is generated for the selected region with grey-scale values shown in the Z-direction axis (figure 4b). The surface plot is composed of 11 line plots 8 μm apart, starting from the right border of the selected region to the left border. In figure 4(b), the first three plots do not intersect the cellular interface and hence do not have many grey-scale fluctuations. The fourth line plot has many sharp peaks, which implies that it intersects the interface at the crest of most waves. Plots 5 and 6 also have many grey-scale fluctuations but many of their peaks are flat peak or dual peak, which implies they intersect the cellular interface, but not at the tip of the crystal cells. Plot 7 looks similar to plot 4, but intersects at the trough of interface waves. The line plot 4, with a one-to-one correspondence between the grey-scale waves and the interface wave, is the ideal plot to determine the interface wavelength. The number of peaks (26, in the example

shown in figure 4(*c*) is counted across the region with a given width (1242.53 μm) to give an average λ (47.8 μm). An ideal line plot can always be obtained by altering the size of the selected region hence varying the distance between adjacent plots.

As the experiment progresses, some crystal cells fall behind and eventually stop growing. A threshold is chosen to determine when to stop counting these trailing cells in calculating the average λ. This threshold, although arbitrary, does give us a standard to compare results of different experiments. Combined with the amplitude measurements described below, any crystal cell whose length or amplitude is less than 70% of the leading cells is not considered. This can be easily implemented by generating a line plot at the 70% position and counting the number of peaks in the plot.

Measuring the amplitude L is much more tedious but less prone to error. As the interface is not a geometric curve with zero thickness, its exact position needs to be determined first. This is achieved by a line plot in the X-direction as shown in figure 4(*d*). The interface position is assumed to occur where the grey-scale plot (in the Z-direction) has the largest negative gradient. Specifically, it is chosen as the midpoint between the largest peak and its next trough in the grey-scale plot. The amplitude L of each crystal cell is defined as the difference in the X-coordinate between its peak and the average of its next two troughs.

4.3. *Planar interface instability*

Before the details of the initial morphological instability of a planar interface are discussed, it is useful to look at the variation of the average wavelength and amplitude as the interface changes from planar to cellular and eventually to dendritic. Growth time t_g is the time the Hele-Shaw cell has been towed. The average cell amplitude L is obtained by averaging the seven leading crystal cells instead of averaging all cells. This is because those crystal cells which have already stopped growing are not contributing to the interface growth any more. When the planar interface just becomes unstable, L increased exponentially (figure 5*a*). This is true until the value of L surpasses the value of λ, which is generally considered as a borderline between the linear regime and the nonlinear regime. After that, nonlinearity plays an important role and L increases with time at a growth speed close to the towing speed. An initial perturbation amplitude L_0 is chosen at the value of 1 μm for all the following experiments. The critical time t_0 is defined as the time when the perturbation amplitude reaches L_0. The critical growth rate σ_0 and critical wavelength λ_0 are the perturbation growth rate and wavelength at t_0, respectively.

The behaviour of L and λ in the linear regime are plotted as functions of t_g in figure 5(*a*). The slope of the linear fitting curve in the $\ln(L)$ vs. t_g plot (figure 5*b*) is the average growth rate σ during the time span covered by those data points. Figure5(*b*) shows that values of σ change significantly if different sets of data points are chosen. For example, if all the data points in the linear regime are chosen, the obtained σ is 0.0223 s^{-1}. If only data points with L less than 10 μm are chosen, σ is 0.0341 s^{-1}. The latter value is believed to be a good approximation for the critical growth rate σ_0. The actual value of σ_0 is probably even larger than this number, but due to the resolving power of the present optical system and recording media, any further improvement in the approximation will be difficult if not impossible. In figure 5(*b*), the critical time t_0 is found by extrapolating the curve in the linear regime to the X-axis, which turns out to be 687 s for the present experiment. In figure 5(*c*), L and λ are plotted as functions of time since the unstable growth began t_u ($t_u = t_g - t_0$), which is a more appropriate

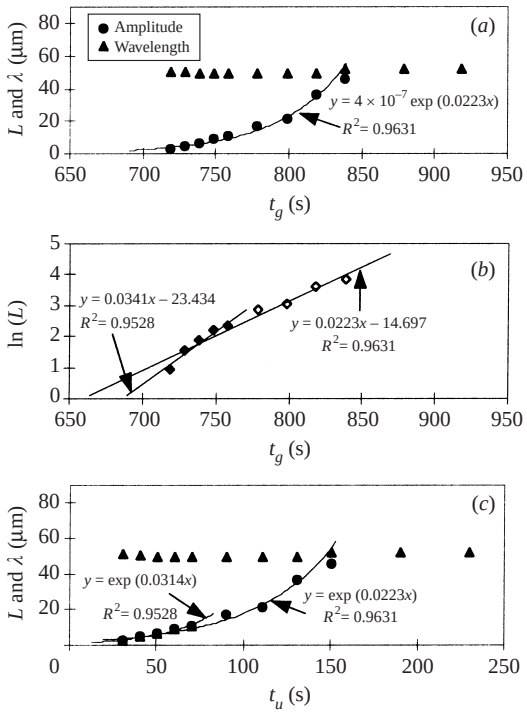

FIGURE 5. No-flow: average amplitude L and wavelength λ in the linear regime of the no-flow experiment ($V' = 3.6\,\mu\mathrm{m\,s^{-1}}$, $G = 7.0\,^{\circ}\mathrm{C\,cm^{-1}}$, R is standard deviation).

time scale for the measurement of growth rate. The equation of each curve is based on the t_0 which is obtained from the corresponding data set in figure 5(b).

Similar results are obtained from experiments with different towing speeds, V', and temperature gradients, G. The values of the dimensionless numbers M and $\mathscr{A}$ are calculated from the interface growth speed V. The same procedure is repeated for all these experiments to obtain the critical λ_0 and σ_0; σ_0 is taken as the average growth rate from the initiation of instability to the point when the average wavelength reaches 10 μm. The difference between this value and the average value over the whole linear regime is larger at the higher growth rates.

The λ_0 and σ_0 are non-dimensionalized by the characteristic length, D/V, and characteristic time, D/V^2. The dimensionless λ^* and σ^* are plotted as functions of M in figure 6. It is shown by both M-S theory and experiment that λ^* increases almost linearly with M, while σ^* decreases with M. This implies that the more unstable interface (larger M) will have longer wavelength but smaller growth rate when it loses its stability. Better agreement is found between theoretical and experimental results for lower morphological numbers, which better satisfy the thermal-steady condition M-S theory assumed.

4.4. *Result of parallel shear flow experiments*

Most theoretical analyses are based on the planar interface growing into a steady flow field, and discuss the conditions at which the interface becomes unstable and once unstable what kind of wave pattern is formed. However, under real experimental conditions, the interface deformation is very small at the onset of the instability and hence the effect of the interface on the flow field is limited. To better understand the

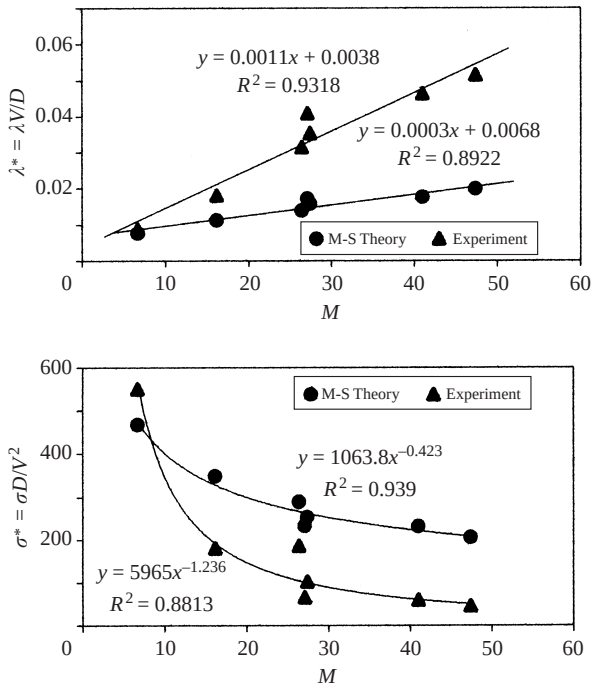

FIGURE 6. No-flow: critical λ^* and σ^* as functions of M.

interactive dynamics between fluid flow and interfacial morphology, three groups of experiments were conducted with the parallel shear flow initiated at different stages of interface growth:

Early-flow experiment: flow was started when the planar interface just became unstable, with crystal cell amplitude $< 10\,\mu$m.

Late-flow experiment: flow was started when the cellular interface was developed, with crystal cell amplitude $> 30\,\mu$m.

Steady-flow experiment: flow was started when the Hele-Shaw cell was stationary. Towing was started after the flow field, thermal field and solid/liquid interface became steady.

The temperature results from these experiments will be discussed first. Then experimental observations are presented. The parallel flow effects are quantified by growth rate, wavelength, interface tilting angle and dendrite tip radius. At the end of the section, a physical mechanism is proposed to explain the observed phenomena.

4.4.1. *Measurement of temperature profiles*

Before experimental observations on the interface variation are presented, results of temperature measurements will be discussed. A thermocouple was placed in the path of the flow (see figure 2). The accuracy of the calibrated thermocouple was 0.1°C, making detection possible for temperature fluctuations caused by the flow larger than 0.1°C. Comparing the data before and after the flow was turned on, it is obvious that the linear temperature distribution inside the Hele-Shaw cell was not noticeably altered by the imposed flow. This situation was achieved by careful adjustment by equalizing the temperature in the surrounding box and the temperature of the local fluid, so that the incoming flow does not become a heat source or heat

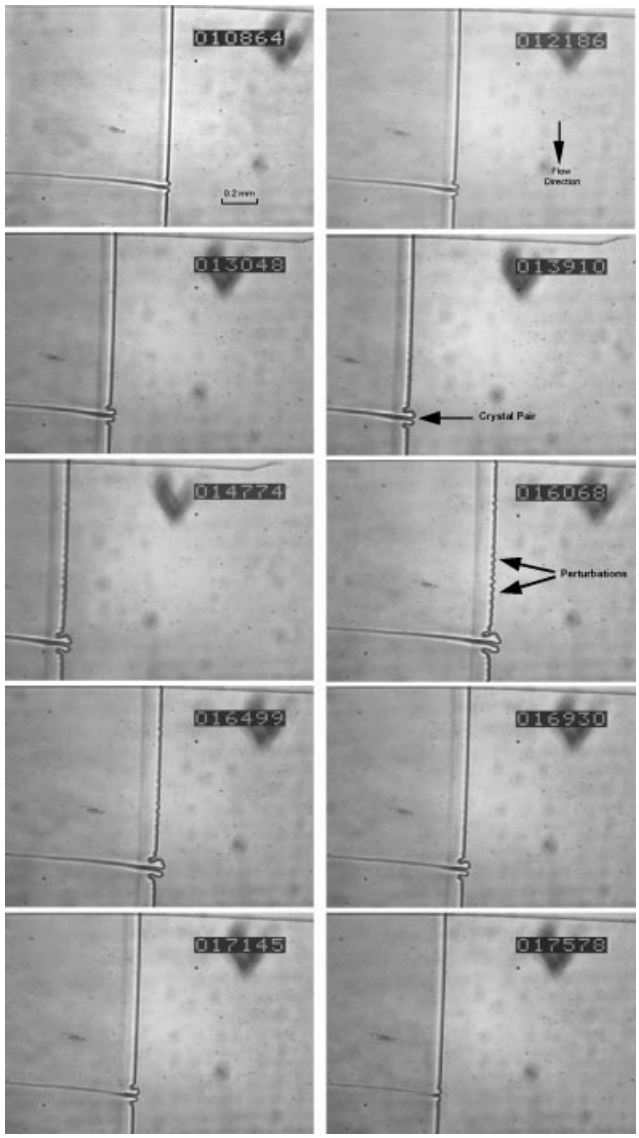

FIGURE 7. Directional solidification: parallel flow applied at an early time (frame 14865) ($V' = 4.5\,\mu\mathrm{m\,s^{-1}}$, $U = 510\,\mu\mathrm{m\,s^{-1}}$, $G = 7.0\,^{\circ}\mathrm{C\,cm^{-1}}$, crystal pair: instability at crystal boundary; perturbations: instability at crystal body).

sink. The reason for doing this is to more closely model the theoretical development by arranging for the flow to move along the isothermal lines. Hence in these two groups of experiments, the effect of flow on interface morphology is mainly from its effect on the concentration field.

4.4.2. *Experimental observations*

Figure 7 shows frames digitized in one early-flow experimental run. The Hele-Shaw cell was towed at $V' = 4.5\,\mu\mathrm{m\,s^{-1}}$ with $G = 7.0\,^{\circ}\mathrm{C\,cm^{-1}}$. The almost horizontal line intersecting the interface is a crystal boundary. The instability was first noticed at the crystal boundary at 6 min (frame 10864). Small perturbations in the crystal body

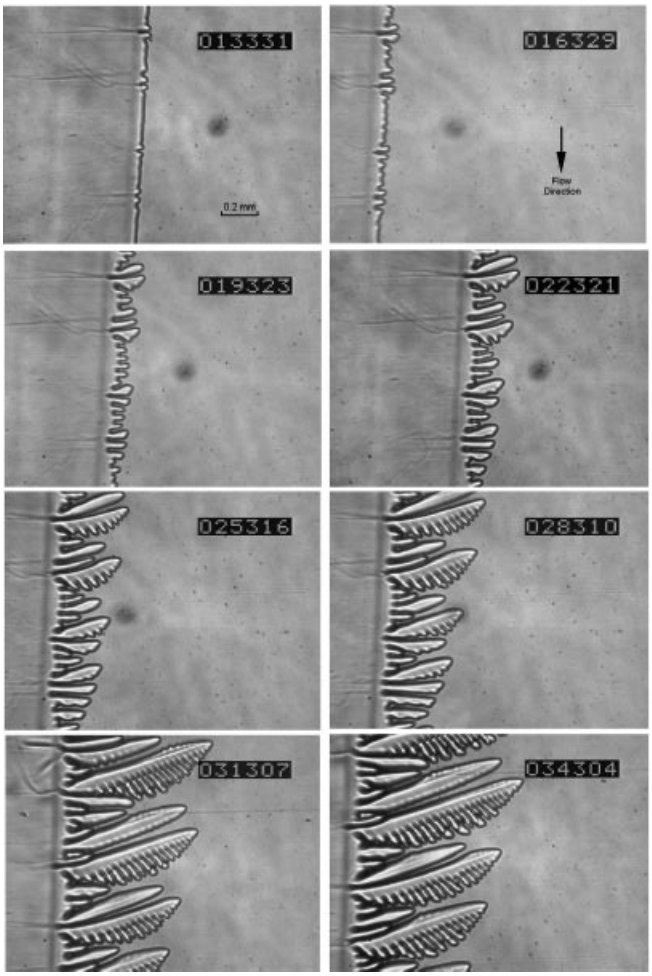

FIGURE 8. Directional solidification: parallel flow applied at a late time (frame 15230) ($V' = 4.6\,\mu\mathrm{m\,s^{-1}}$, $U = 510\,\mu\mathrm{m\,s^{-1}}$, $G = 7.0\,^{\circ}\mathrm{C\,cm^{-1}}$).

appeared at 8.2 min (frame 14774). The flow was imposed at 8.3 min (frame 14865) when the amplitude of the sequence of perturbations was still very small ($< 10\,\mu$m). The flow direction is from top to bottom in figure 7 and the free-stream flow speed U is $510\,\mu\mathrm{m\,s^{-1}}$. It is interesting to note that after the flow is imposed, the cellular crystals continue to grow for a short period of time until 8.9 min (frame 16068) and then decay rapidly. At 9.4 min (frame 16930), perturbations are almost indiscernible. The crystal pair, which originated from the crystal boundary and has a larger amplitude ($36\,\mu$m) when flow starts, also demonstrates the same behaviour, although at a different decay rate. Experiments were repeated for different towing speeds V' and with flow in the reversed direction, while holding U and G fixed. The same stabilizing behaviour was observed and recorded for all the experiments.

Figure 8 shows results from one late-flow experiment. The flow direction is also from top to bottom with the same flow strength as the previous experiment. The flow was turned on at 8.5 min (frame 15230) for this particular experimental run. Unlike the decay observed in the previous experiment, small cellular structures started tilting toward the upstream direction (frame 19323). At 12.4 min (frame 22321), the

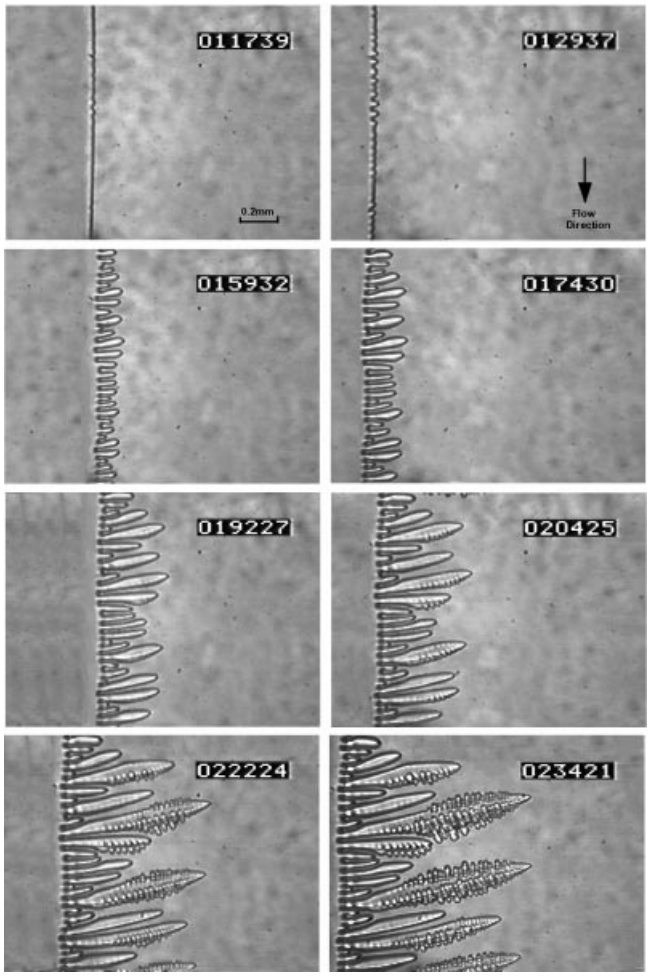

FIGURE 9. Directional solidification: steady parallel flow (frame 0) ($V' = 3.8\,\mu\mathrm{m\,s^{-1}}$, $U = 830\,\mu\mathrm{m\,s^{-1}}$, $G = 7.1\,^{\circ}\mathrm{C\,cm^{-1}}$).

secondary branch appeared on the downstream side of the leading crystals while the other crystals were suppressed. The crystals continued growing into the flow as the tilting angle increased until it reached some steady value and kept growing in the direction of that tilting angle (frame 31307 and 34304). Similar results were obtained when experiments were repeated at various towing speeds and flow directions.

Figure 9 shows results from one steady-flow experiment with the temperature gradient as in the previous two experiments but different V' ($3.8\,\mu\mathrm{m\,s^{-1}}$) and U ($830\,\mu\mathrm{m\,s^{-1}}$). The flow is steady through the entire experiment and the flow direction is from top to bottom. The frame sequence in figure 9 looks similar to that seen in the late-flow experiment (figure 8). After crystal cells formed, they grew in a direction tilting into the flow (frame 15932, 17430 and 19227). The secondary branch appeared first on the downstream side (frame 20425) and later appeared on the upstream side as well (frame 22224), whereas in the late-flow experiments, secondary dendrites did not appear on the upstream side even at a much later stage of the cell–dendrite transition.

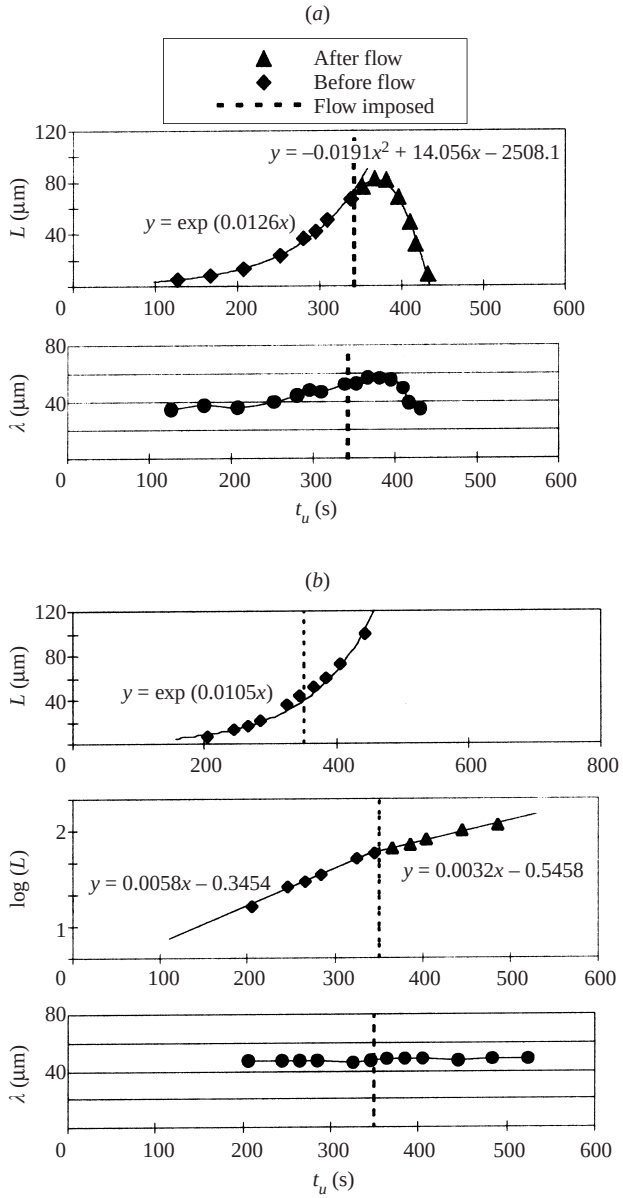

FIGURE 10. Effect of parallel shear flow on amplitude growth rate and wavelength ($V' = 4.6\,\mu\mathrm{m\,s^{-1}}$, $U = 510\,\mu\mathrm{m\,s^{-1}}$, $G = 7.0\,^{\circ}\mathrm{C\,cm^{-1}}$). (*a*) Early-flow (amplitude of leading crystal cells plotted to avoid measurement uncertainty). (*b*) Late-flow (average amplitude of crystal cells plotted).

4.4.3. *Effect of parallel shear flow on growth rate and wavelength*

In order to further study the parallel shear flow effect quantitatively, the amplitude and the wavelength of the cellular interface were measured at different growth times for each experimental run.

Figure 10(*a*) shows the case when the flow was imposed at an early time in the growth. The amplitude of the crystal pair which grew from the crystal boundary is measured and plotted here, to avoid a large experimental uncertainty in measuring the amplitude of the shallow crystal cells. It is shown that prior to initiating the

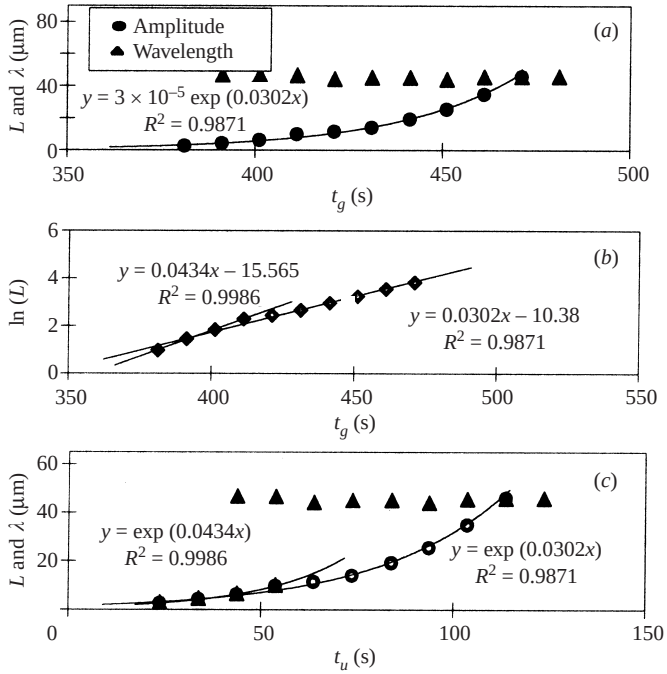

FIGURE 11. Steady parallel shear flow: average wavelength and cell amplitude in the linear regime ($V' = 4.5\,\mu\mathrm{m\,s^{-1}}$, $U = 510\,\mu\mathrm{m\,s^{-1}}$, $G = 7.0\,^{\circ}\mathrm{C\,cm^{-1}}$, t_g is growth time, t_u is unstable time).

flow, the crystal amplitude grew exponentially with a growth rate of $0.0126\,\mathrm{s^{-1}}$. Once the flow was imposed, the growth rate was greatly reduced. After 26 s, the amplitude decayed rapidly at a rate of $\mathrm{d}L/\mathrm{d}t = -1.02\,\mu\mathrm{m\,s^{-1}}$. Amplitude data for shallow crystal cells were also measured and plotted, displaying a similar trend as the crystal pair, but on a much smaller scale. The effect of flow on wavelength is not as prominent as the effect on amplitude. The data obtained from the shallow cells shows that the wavelength is nearly invariant before and after the start of the flow.

Figure 10(b) shows the case of late-flow experiments. It is difficult to quantify the difference in the amplitude–time plot before and after the flow was induced. But the difference is noticeable in a log(L) vs. time plot. The exponential growth rate (slope of log(L) vs. time curve) is slightly reduced after the initiation of the flow. However, whether this growth rate reduction is solely from the effect of parallel flow or not is still an open question, because the nonlinearity could play a role in slowing down the growth (for the subcritical bifurcation) as the amplitude becomes larger and larger.

As in the early-flow experiments, the trend of the flow effect on wavelength is small. This is evidenced by the fact that some experiments show invariance in wavelength, some show small fluctuations, and other show monotonic increase. But all experiments demonstrate that the variance of wavelength is smaller than 10 μm. Therefore, we conclude that the wavelength of the cellular interface is insensitive to the imposed parallel flow.

Average wavelength and average cell amplitude are measured at different growth times t_g. The average L is obtained by averaging over 8 leading crystals rather than averaging over all crystal cells, because the former average can better represent the interface growth. The changes in L and λ are shown expanded for the linear regime in figure 11. The critical amplitude and growth rate for the experiment shown in figure 9 are found to be 46.3 μm and $0.0434\,\mathrm{s^{-1}}$, respectively.

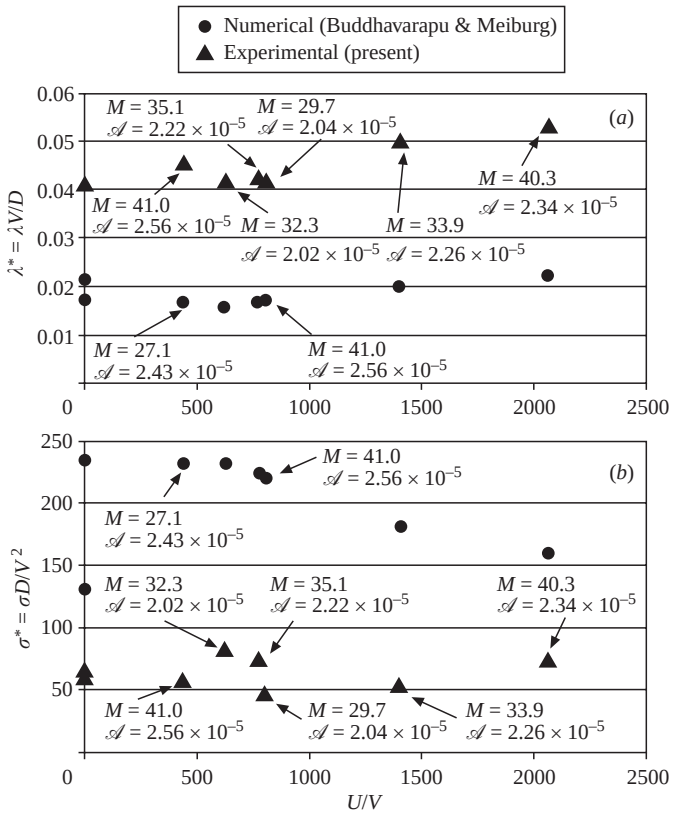

FIGURE 12. Steady parallel shear flow: critical λ and σ as functions of velocity ratio U/V.

To systematically study the flow effect on the critical point, experiments were conducted for different velocity ratios, U/V. Ideally the morphological number M and surface parameter $\mathscr{A}$ are held fixed, and only the flow speed changed. However, the interface growth speed V is affected by the change of flow speed U, even at the same towing speed. As a result, M and $\mathscr{A}$, which are functions of V, are practically impossible to control.

The experimental results for dimensionless wavelength λ^* and dimensionless growth rate σ^* are compared with numerical results of Buddhavara & Meiburg (2002, part 2 of this work) in figure 12. Values of M and $\mathscr{A}$ for each experiment are put next to the data point. In figure 12(a) and figure 12(b), no obvious trend is noticed in either experimental data or numerical result; this could because the effect of flow speed change is overwhelmed by the effect of M and $\mathscr{A}$.

4.4.4. *Effect of parallel shear flow on interface tilting angle*

Since no crystal tilting was observed in the early-flow experiments, results regarding the parallel flow effect on crystal tilting are based on the late-flow experiments. The tilting angle ψ is defined as the angle from the normal direction of the initial planar interface, at which crystals grow steadily. The tilting angles at different U/V ratio are plotted in figure 13(a). It is noted that crystals tilt more at higher U/V. This trend can be explained by the effect of solute transport in the liquid on crystal growth. During the directional solidification process, there are two solute transport processes competing with each other: lateral solute transport which is characterized by the free-stream

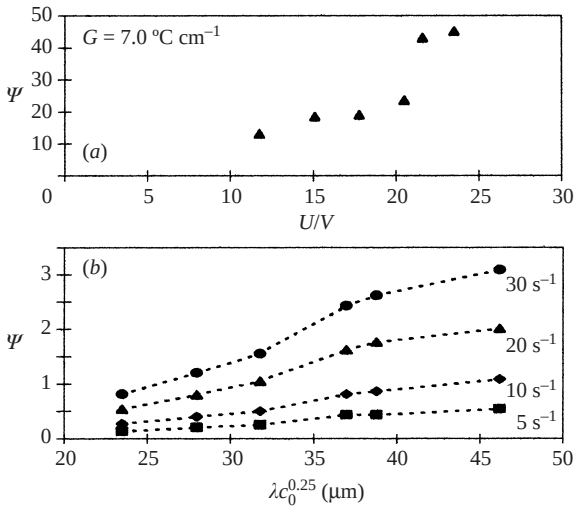

FIGURE 13. Steady parallel share flow: tilting angle of crystals for various processing conditions. Note: here U is made dimensionless with the speed of propagation of the tips of the dendrites, which is equal to the towing speed in this limit.

velocity U, and the normal solute rejection or solute transport which is characterized by the towing speed V. Higher U/V gives a higher degree of asymmetry in the solute distribution around the crystal tips, and results in larger crystal tilting angles.

The same problem was considered by Dantzig & Chao (1986, 1990). Although their computational results are based on another dilute alloy, Sn–1.0 Wt% Pb, it is a good reference with which to qualitatively compare results. The tilting angles ψ are shown in figure 13(b) for different conditions, where λ is the characteristic length and can be chosen to be the wavelength, C_0 is the concentration of the sample alloy, the numbers listed next to the curves are the shear rate (flow speed) with units s^{-1}. There is no special significance to the scaling exponent 0.25. For the same flow and same composition, tilting angles increase with the wavelength. For the same wavelength and same composition, crystals demonstrate the same behaviour as obtained in our experiments: tilting angles monotonically increase with flow speed.

4.4.5. *Possible physical mechanisms to explain the present results*

A possible physical mechanism to explain our experimental results is a parallel shear flow model, much like that discussed by Dantzig & Chao. Since the thermal transport is not affected by the forced parallel flow (as shown in §4.1), the flow influences the interface morphology by altering the solute transport.

In the no-flow directional solidification case, some sections of the interface may have a greater solute concentration than other sections. As a result of local freezing temperature reduction, these sections will have slower growth rates and will become troughs in the cellular interface. This lateral solute inhomogeneity drives the interfacial instability. When the parallel shear flow is applied at an interface with small amplitudes ($< 10\,\mu$m in the experiment), the flow field is minimally altered by the shallow crystal cells and is still locally parallel to the interface (figure 14a). This local parallel flow dramatically enhances the lateral solute transport. Therefore the early parallel flow stabilizes the interface by smoothing out the lateral solute inhomogeneity at the interface. This stabilizing effect is apparent in figure 7. Similar results were observed from other experiments with different towing speeds.

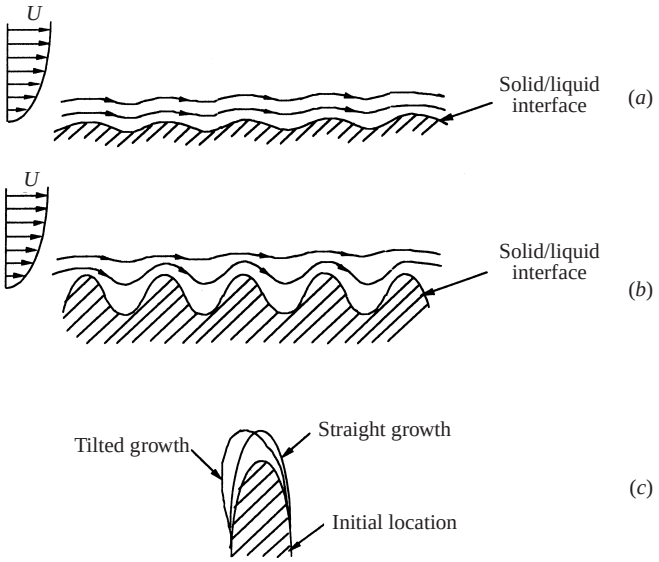

FIGURE 14. Physical mechanisms for the effect of parallel shear flow on interfacial morphology: (*a*) shallow cell; (*b*) deep cell; (*c*) tilting cell.

However, the same externally imposed flow gives a different effect if it is imposed at a later time. When the parallel shear flow is applied at the deep cellular interface, the flow field is distorted by the periodic curved interface (figure 14*b*). In the absence of flow, the concentration field is symmetric with respect to the centreline of each cell. Flow has a stronger compressing effect on the upstream side of crystal cells than on the downstream side, which leads to an asymmetry in the concentration field with a thinner solutal boundary layer, and hence greater G_c at the upstream side. Therefore, the upstream side of the cell has a higher normal growth rate than the downstream side and as a result the cell tilts toward the incoming flow direction (figure 14*c*).

The parallel flow velocity at the interface can be decomposed into two parts, according to their direction with respect to the interface. The lateral component tends to transport the non-uniform solute and hence stabilizes the interface. The normal component tends to compress the solutal boundary layer and hence destabilizes the interface. It is the combined effect that determines the interface behaviour.

In the early-flow experiments, the lateral transport effect is much stronger than the normal compressing effect, therefore the stabilizing effect is dominant. In the late-flow experiments, where the normal compressing effect becomes stronger, tilting crystal cells are found. However, the mixing effect is still present in the late-flow experiments, and this effect is also asymmetric since it is much stronger at the upstream side than the downstream side. This explains why the secondary branches only appears on the downstream side.

5. Conclusions

Directional solidification experiments have been carried out in a Hele-Shaw cell with and without externally imposed parallel shear flows over the solid/liquid interface. The specimen material used was transparent organic alloy SCN–1.0 Wt% acetone. The experiment process was observed *in-situ* using an interference microscope.

Pure morphological experiments were conducted to serve as a comparison for experiments with flows. New methods were developed to better measure the shape

and position of the solid/liquid interface. The experimental result agrees with M-S theory in finding that the critical wavelength increases with morphological number M while the critical growth rate decreases with M. Theoretical and experimental results were found to be in better agreement when M is smaller.

The initiation time of the parallel shear flow was varied in different sets of experiments. The flow was started when the planar interface just became unstable, when the cellular interface was fully developed, as well as a long time before directional solidification began. The experiment was adjusted so that the heat source or sink effect convected by the parallel flow could be neglected.

The comparison of experimental data shows that the transient parallel flow has a stabilizing effect on the planar interface by damping existing initial perturbations. This observation seems to agree well with findings by Tewari & Chopra (1992) and Kauerauf *et al.* (1998) in Pb–Sn and Succinonitrile–acetone where the onset of interfacial breakdown was delayed by the presence of convection.

Transient parallel flow also shows a stabilizing effect on the cellular interface by slightly reducing the exponential growth rate of crystal cells. However, no obvious conclusion can be drawn for steady parallel flow based on the experimental finding that neither critical wavelength nor critical growth rate of perturbations are sensitive to either the existence or the strength of the flow.

The left–right symmetry of crystal cells was broken by the parallel flow with cells tilting toward the incoming flow direction. The tilting angle increased with the velocity ratio (flow speed over interface growth speed). Secondary dendrites were found either not to appear or to appear much later on the downstream side of the cells. The wavelengths of the initial perturbations and of the cellular interface were insensitive to the imposed flow.

The experimental results can be explained qualitatively through the parallel flow effect on lateral solute transport. The phenomenon of crystal cells tilting against the flow is consistent with the numerical result of Dantzig & Chao. The result that the tilting angle increases with the non-dimensional flow velocity also agrees with theirs, despite the fact that different alloys were considered. It is proposed that there is a coupling effect between the interfacial morphology and the imposed parallel shear flow. Different effects of the interfacial morphology on the imposed flow lead to different effects of the imposed flow on the interface, and vice versa.

Informative discussions with Professors S. H. Davis of Northwestern University and E. Meiburg of U.C. Santa Barbara are gratefully acknowledged. This work was supported by the NASA Microgravity Program under Grant number NAG8-1240.

REFERENCES

Brattkus, K. & Davis, S. H. 1988*a* *J. Cryst. Growth* **87**, 385.

Brattkus, K. & Davis, S. H. 1988*b* *J. Cryst. Growth* **89**, 423.

Buddhavarapu, S. S. & Meiburg E. 2002 *J. Fluid Mech.* **470**, 269.

Caroli, B., Caroli, C. & Roulet, B. 1986 *J. Cryst. Growth* **76**, 31.

de Cheveigne, S., Guthmann, C. & Lebrun, M. M. 1986 *J. Phys. Paris* **73**, 242.

Chopra, M. A., Glicksman, M. E. & Singh, N. B. 1988*a* *J. Cryst. Growth* **92**, 543.

Chopra, M. A., Glicksman, M. E. & Singh, N. B. 1988*b* *Metall. Trans.* A **19**, 3087.

Coriell, S. R. & McFadden, G. B. 1993 Morphological stability. In *Handbook of Crystal Growth* (ed. D. T. J. Hurle), vol. 1b, chap. 12, p. 787. Elsevier.

Coriell, S. R., McFadden, G. B., Boisvert, R. F. & Sekerka, R. F. 1984 *J. Cryst. Growth* **69**, 15.

Dantzig, J. A. & Chao, L. S. 1986 The effect of shear flows on solidification microstructure. *Proc. Tenth US Natl Cong. Appl. Mech.* p. 249. ASME.

Dantzig, J. A. & Chao, L. S. 1990 Fluid flow and microstructure development *Proc. Intl Symp. on Solidification Proc.* p. 12.

Delves, R. T. 1968 *J. Cryst. Growth* **3,4**, 562.

Delves, R. T. 1971 *J. Cryst. Growth* **8**, 13.

Eshelman, M. A., Seetharaman, V. & Trivedi, R. 1988 *Acta Metall.* **36**, 1165.

Eshelman, M. A. & Trivedi, R. 1987 *Acta Metall.* **35**, 2443.

Flemings, M. C. 1974 *Solidification Processing*. McGraw-Hill.

Forth, S. A. & Wheeler, A. A. 1989 *J. Fluid Mech.* **202**, 339.

Forth, S. A. & Wheeler, A. A. 1992 *J. Fluid Mech.* **236**, 61.

Huang, T., Liu, S., Yang, Y., Lu, D. & Zhou, Y. 1993 *J. Cryst. Growth* **128**, 167.

Jackson, K. A. & Hunt, J. D. 1965 *Acta Metall.* **13**, 1212.

Kauerauf, B., Zimmermann, G., Murmann, L. & Rex, S. 1998 *J. Cryst. Growth* **193**, 701.

Kurz, W. & Fisher, D. J. 1981 *Acta Metall.* **29**, 11.

Lan, C. W., Chen, M. K. & Liang, M. C. 1998 *J. Cryst. Growth* **187**, 303.

Lee, J. T. C. & Brown, R. A. 1993 *Phys. Rev.* B **47**, 4937.

Merchant, G. J. & Davis, S. H. 1989*a J. Cryst. Growth* **96**, 737.

Merchant, G. J. & Davis, S. H. 1989*b Phys. Rev. Lett.* **63**, 573.

Mullins, W. W. & Sekerka, R. F. 1964 *J. Appl. Phys.* **35**, 444.

Rubinstein, E. R., Tirmizi, S. H. & Glicksman, M. E. 1990 *J. Cryst. Growth* **106**, 89.

Schulze, T. P. & Davis, S. H. 1995 *J. Cryst. Growth* **149**, 253.

Tewari, S. N. & Chopra, M. A. 1992 *J. Cryst. Growth* **118**, 183.